



Contents lists available at ScienceDirect

## Sensors and Actuators: B. Chemical

journal homepage: [www.elsevier.com/locate/snb](http://www.elsevier.com/locate/snb)

### 3-Dimensional electrical impedance spectroscopy for *in situ* endoluminal mapping of metabolically active plaques

Parinaz Abiri<sup>a,b,1</sup>, Yuan Luo<sup>c,g,1</sup>, Zi-Yu Huang<sup>d,1</sup>, Qingyu Cui<sup>a,1</sup>, Sandra Duarte-Vogel<sup>e</sup>, Mehrdad Roustaei<sup>b</sup>, Chih-Chiang Chang<sup>b</sup>, Xiao Xiao<sup>b</sup>, Rene Packard<sup>a</sup>, Susana Cavallero<sup>a</sup>, Ramin Ebrahimi<sup>a</sup>, Peyman Benharash<sup>f</sup>, Jun Chen<sup>b</sup>, Yu-Chong Tai<sup>d</sup>, Tzung K. Hsiai<sup>a,b,d,\*</sup>

<sup>a</sup> Division of Cardiology, Department of Medicine, David Geffen School of Medicine, University of California, Los Angeles, Los Angeles, CA 90095, USA

<sup>b</sup> Department of Bioengineering, University of California, Los Angeles, Los Angeles, CA 90095, USA

<sup>c</sup> State Key Laboratory of Transducer Technology, Shanghai Institute of Microsystem and Information Technology, Chinese Academy of Sciences, Shanghai 200050, China

<sup>d</sup> Department of Medical Engineering, California Institute of Technology, Pasadena, CA 91125, USA

<sup>e</sup> Division of Laboratory Animal Medicine, University of California, Los Angeles, Los Angeles, CA 90095, USA

<sup>f</sup> Division of Cardiac Surgery, Department of Surgery, David Geffen School of Medicine, University of California, Los Angeles, Los Angeles, CA 90095, USA

<sup>g</sup> Center of Materials Science and Optoelectronics Engineering, University of Chinese Academy of Sciences, Beijing 100049, China

## ARTICLE INFO

## Keywords:

Electrical impedance spectroscopy (EIS)  
Electrical impedance tomography (EIT)  
Intravascular microelectrode array  
3-D histology for conductivity modeling  
Metabolically active plaque

## ABSTRACT

Electrical impedance spectroscopy (EIS) has been recognized to characterize oxidized low-density lipoprotein (oxLDL) in the metabolically active plaque. However, intravascular deployment of 3-D EIS-derived electrical impedance tomography (EIT) for endoluminal mapping of oxLDL-laden arterial walls remains an unmet clinical challenge. To this end, we designed the 6-point microelectrode arrays that were circumferentially configured onto the balloon catheter for 15 intravascular EIS permutations. In parallel, we created the metabolically active plaques by performing partial ligation of right carotid artery in Yorkshire mini-pigs ( $n = 6$  males), followed by demonstrating the plaque progression at baseline, 8 weeks, and 16 weeks of high-fat diet via computed tomography (CT) angiogram. Next, we deployed the 3-D EIS sensors to the right and left carotid arteries, and we demonstrated 3-D EIS mapping of metabolically active endolumen in the right but not left carotid arteries as evidenced by the positive E06 immunostaining for oxLDL-laden regions. By considering electrical conductivity ( $\sigma$ ) and permittivity ( $\epsilon$ ) properties of collagen, lipid, and smooth muscle presence in the arterial wall, we further validated the 3-D EIS-derived EIT by reconstructing the histology of right and left carotid arteries for the finite element modeling of the oxLDL-laden endolumen, and we accurately predicted 3-D EIS mapping. Thus, we establish the capability of 3-D EIS-derived EIT to detect oxLDL-laden arterial walls with translational implication to predict metabolically active plaques prone to acute coronary syndromes or stroke.

#### 1. Introduction

Electrical impedance spectroscopy (EIS) detects oxidized low-density lipoprotein (oxLDL)-laden plaques [1–3], and oxLDL promotes metabolically active plaque to rupture, leading to acute coronary syndromes or stroke [4–8]. Diagnostic results obtained from histology, intravascular ultrasound (IVUS), and optical coherence tomography (OCT) support that high-oxLDL content predicts the metabolically active plaques [9–15]. Despite the advances in computed tomographic (CT)

angiography [16], high resolution MRI [17], IVUS [18], near-infrared fluorescence (NIRF) [19], and time-resolved laser-induced fluorescence spectroscopy (LIF) [20], endoluminal mapping of oxLDL-laden arteries remains an unmet clinical need to predict metabolically unstable plaque.

We and others have previously demonstrated that an increase in the frequency-dependent impedance develops in the oxLDL-rich aortic walls [2,3,21–23]. Lipid-free arterial wall is an efficient electrical conductor due to its high water (approximately 73%) and electrolyte (ions and

\* Correspondence to: Department of Bioengineering and Division of Cardiology, Center for Health Sciences, CHS 37-2000G, 65 Charles Young Dr, University of California, Los Angeles, Los Angeles, CA 90073, USA.

E-mail address: [THsiai@mednet.ucla.edu](mailto:THsiai@mednet.ucla.edu) (T.K. Hsiai).

<sup>1</sup> These authors contributed equally to this work.

<https://doi.org/10.1016/j.snb.2021.131152>

Received 21 September 2021; Received in revised form 17 November 2021; Accepted 23 November 2021

Available online 29 November 2021

0925-4005/© 2021 The Authors.

Published by Elsevier B.V. This is an open access article under the CC BY-NC-ND license

(<http://creativecommons.org/licenses/by-nc-nd/4.0/>).

proteins) content, whereas lipid-rich wall is anhydrous and thus, a poor conductor. When an alternative current (AC) stimulation is applied to the arterial plaque, electric impedance ( $Z$ ) is acquired as a function of frequency.  $Z$  is defined as the summation of the resistance ( $R$ ) and reactance ( $X$ ) multiplied by a complex number,  $i$  ( $Z = R + iX$ ). By recording the endoluminal impedance from 10 to 1000 kHz, the electrical and dielectric properties can be determined [2]. Thus, the frequency-dependent EIS of the oxLDL-laden plaque is significantly elevated as compared to the oxLDL-free arterial walls between 10 kHz to 100 kHz [1].

To this end, we sought to demonstrate 3-D EIS-derived electrical impedance tomography (EIT) for *in situ* endoluminal mapping of carotid arterial walls in a pre-clinical swine model. We designed 3-D EIS sensors by configuring 6-point microelectrode array on a balloon catheter, allowing for 15 permutations of intravascular EIS measurements. Next, we developed oxLDL-rich plaques in the Yucatan mini-pigs via partial ligations of right carotid arteries. After 16 weeks of high-fat diet, we deployed the EIS catheter to the carotid arteries for 3-D EIS mapping. The low conductivity regions in the arterial walls corresponded to the positive immunostaining (E06) for oxLDL in the right but not left carotid arteries. We further reconstructed the 3-D histologic features of the carotid arteries for finite element modeling of impedance by considering electrical conductivity ( $\sigma$ ) and permittivity ( $\epsilon$ ) properties of collagen, lipid, and smooth muscle presence in the arterial wall. We demonstrated the capability of our 3-D histology-derived finite element modeling to predict and validate 3-D EIS mapping. Thus, we establish 3-D EIS-derived EIT mapping to detect oxLDL-laden arterial walls that holds promises for early detection of metabolically active plaques prone to develop acute coronary syndromes or stroke.

## 2. Materials and methods

### 2.1. Development and integration of flexible 3-D microelectrode array

A catheter-based electrical impedance spectroscopy (EIS) sensor (7F diameter) was developed for intravascular delivery and endoluminal

mapping (Fig. 1A and B). Custom-designed flexible polyimide electrodes (600  $\mu\text{m}$  x 300  $\mu\text{m}$ ) (FPCexpress, Canada) were affixed onto the balloon catheter via silicon adhesive for EIS measurements. Six of these electrodes were positioned in two rows (3 by 3 electrodes) at 1.4 mm apart along the circumference of an inflatable balloon of 9 mm in length (low-durometer urethane Ventiona Medical, NH), and the inflatable diameters of the balloon ranged from 2 to 10 mm (Fig. 1C). The electrodes in contact with the endolumen generated electrical field for intravascular EIS measurements. The equivalent circuit reveals the 6-point electrodes for 15 permutations (Fig. 1D).

The balloon was coaxially inserted into the distal end of a polyethylene catheter (Vention Medical, NH), and was anchored with the epoxy glue. Micro holes were created on the catheter for balloon inflation (Figs. 2A and 2B). The catheters were insulated with heat-shrink tubing (Vention Medical, NH). A pair of tantalum foils (Advanced Research Materials, UK) was added to both ends of the balloon as radiopaque markers for visualization during fluoroscope. The electrical conduction to the impedance analyzer was connected by soldering a joint between the copper wires (26 AWG) and contact pads at the terminal end of the flexible electrodes. The electrodes were electroplated with platinum black (Sigma-Aldrich) to increase the junction capacitance and to enhance the accuracy of two-point electrode measurements (see Supplementary Figure S-4).

### 2.2. Creating a swine model of metabolically active plaque

A combination of high-fat diet and partial carotid arterial ligation was previously demonstrated to promote atherosclerotic plaques in a swine model [24]. We performed partial ligation to the right carotid arteries (Fig. 3). Detail surgical procedures for partial carotid ligation are available in Supplementary (SI-1). The animal study was approved by the UCLA Animal Research Committee in compliance with the institutional IACUC protocols. The surgical procedures and the post-operative care were performed by experienced veterinarians from the Division of Laboratory Animal Medicine at UCLA School of Medicine. The surgical wound was closed layer by layer to avoid manipulation to

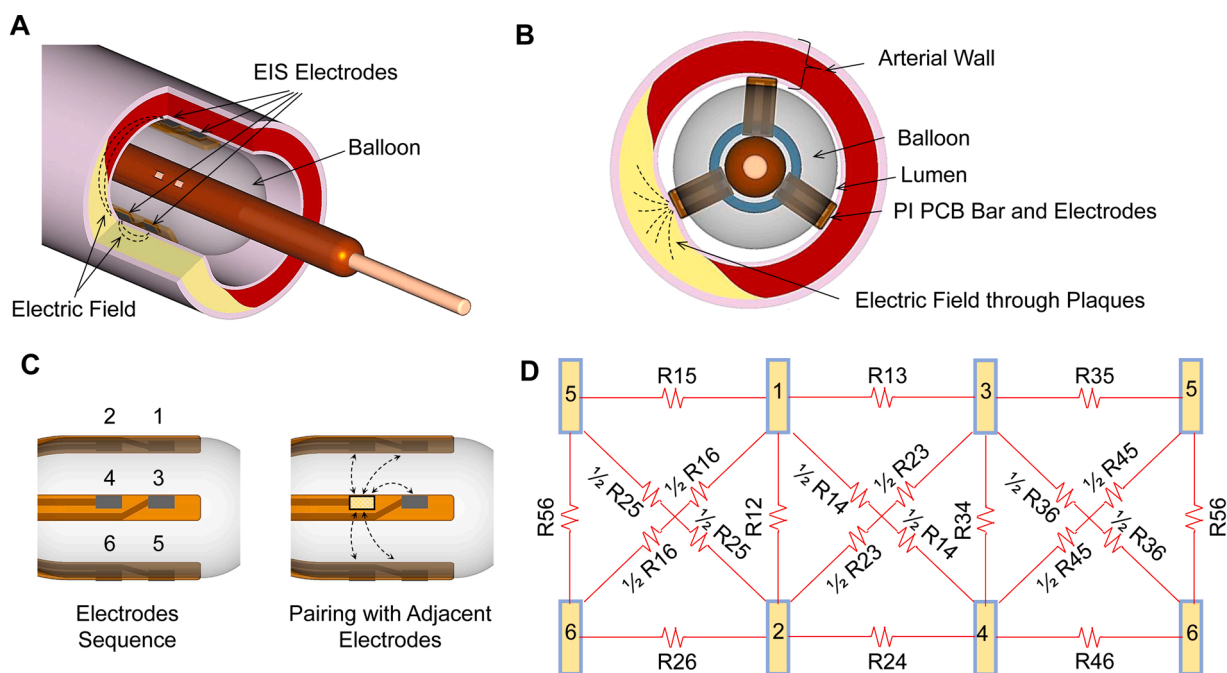


**Fig. 1.** 6-Point Microelectrode Configuration to Interrogate the Plaque. (A) The flexible 6-point electrodes were affixed on the balloon. (B) A cross-sectional view shows the inflated balloon in relation to the eccentric atherosclerotic plaque. The electrodes in contact with the endolumen generated electrical field from EIS measurements. (C) The flexible polyimide and electrodes were configured for the 6-point arrangement, generating 15 permutations. (D) The equivalent circuit reveals the 6-point electrodes and the 15 pairs of electrodes for EIS measurements.

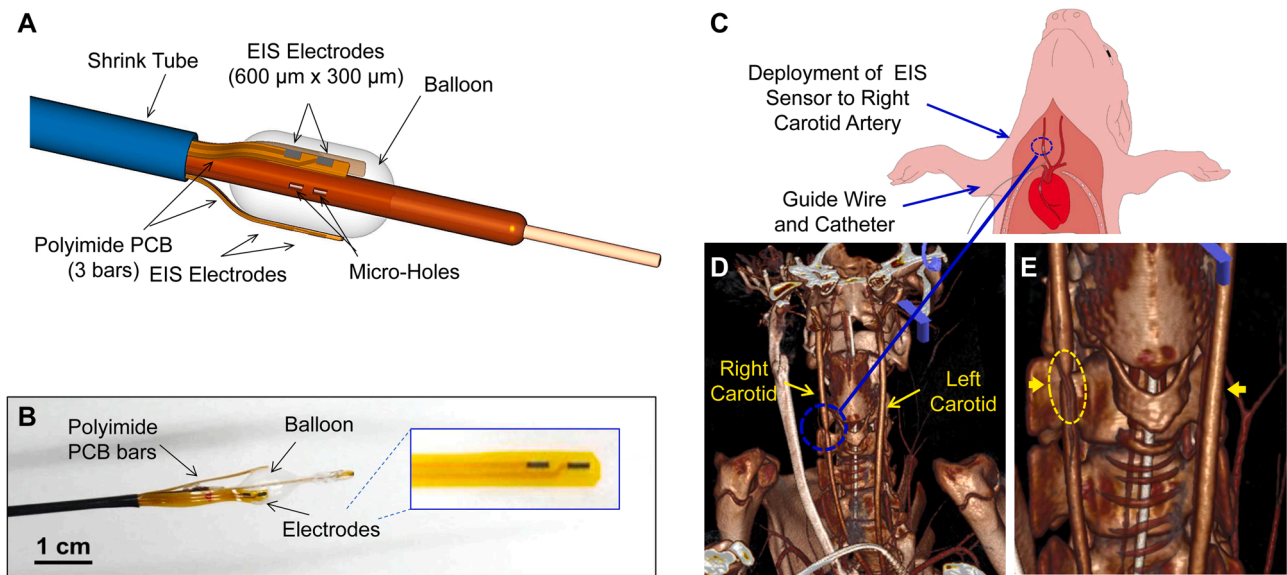


**Fig. 2.** Intravascular deployment of the 3-D 6-point microelectrodes. (A) Schematic demonstrates the balloon catheter-based microelectrode array affixed onto the balloon catheter. The flexible polyimide electrodes (600 μm x 300 μm) connects with the 3 polyimide PCB bars to the external impedance analyzer. Micro holes were opened on the catheter for balloon inflation. (B) A photo of the balloon catheter reveals the microelectrodes connected to the polyimide. A pair of tantalum foils was added to both ends of the balloon as radiopaque markers. (C) An anatomic depiction of the heart and the 3-D sensor deployment to the right carotid artery in a swine model. (D) A 3-D CT scan depicts the right carotid artery following partial ligation in comparison to the left. (E) An enlargement of the 3-D CT scan reveals the narrowing of the right carotid artery (dotted circle) following 16 weeks of high-fat diet.

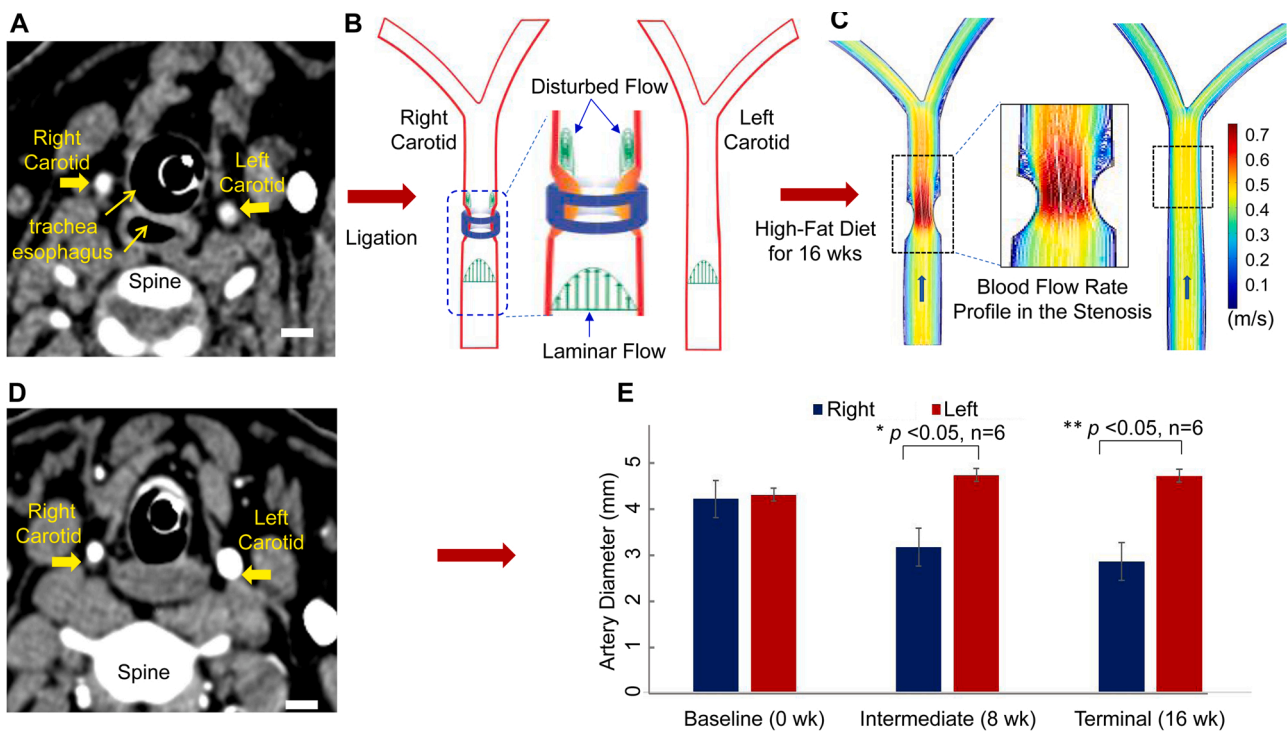


**Fig. 3.** Development of oxLDL-Laden Right Carotid Arteries in the Yucatan mini-pigs. (A) Cross-sectional (terminal axial) CT scan at baseline reveals right and left carotid arteries in relation to the spine, trachea, and esophagus of the Yucatan mini-pig. (B) Partial ligation of right carotid artery promotes disturbed flow downstream from the narrowing or stenosis. Disturbed flow is well-recognized to prime the development of plaque formation or atherosclerosis. (C) Doppler ultrasound provides the inlet and outlet velocity to perform computational fluid dynamics (CFD) simulation across the stenosis. (D) CT scan at 16 weeks of high-fat diet indicates narrowing or stenosis of the right carotid arteries in comparison to the left. (E) Comparison between the mean right and left carotid diameters at 0 weeks (baseline), 8 weeks post-surgery (intermediate), and 16 weeks post-surgery (terminal) demonstrates development of significant stenosis at the intermediate and terminal time ( $p < 0.05$ ,  $n=6$ ).

the adjacent tissues. The animals were allowed for recovering after surgery, and they were resumed to the high-fat diet for 16 weeks (Test Diet; Purina, St. Louis, MO). Serial aortic CT angiograms were

performed to demonstrate the reduction in the diameters of the carotid arteries following iodinated contrast injection to the tail vein at baseline, 8 weeks, and 16 weeks. Next, we deployed the 3-D microelectrodes to

the right (partial ligation) and left (sham) carotid arteries in the Yucatan miniature pigs ( $n = 6$ , 20-30 kg, S & S Farms, Ranchita, CA), and we created the narrowing of the carotid arteries as a result of oxLDL-laden plaque downstream from the carotid ligation where disturbed flow, also known as oscillatory shear stress, developed to promote plaque formation [24,25].

### 2.3. Intravascular 3-D flexible microelectrodes to interrogate lipid-rich arterial wall

The deployment of 3-D microelectrodes for intravascular EIS measurements of oxLDL-laden arterial is represented by the schematic diagram (Fig. 2C). To deploy the microelectrode array for 3-D EIS measurements, the animals were anesthetized as described above (see Supplementary SI-1). The 6-point microelectrodes were advanced to the level of the stenosis in the right carotid arteries, along with the radiopaque markers under fluoroscopic guidance (Siemens Artis Zeego with robotic arm), and iodinated contrast dye was injected into the vessel for visualization of the 3-D EIS sensor.

Next, the balloon with the six circumferentially fixed electrodes was inflated to a constant pressure of  $\sim 14$  psi via a mechanical pump so that the microelectrodes were in contact with the endoluminal surface (Fig. 1B). Endoluminal EIS measurements were conducted using the Gamry system (Gamry Series G 300 potentiostat, USA) in which fifteen scans for each EIS sensor were performed based on 15 paired combinations between the six electrodes (Fig. 1C-D). A peak-to-peak voltage of 50 mV was delivered to acquire the frequency-dependent impedance profiles ranging from 1 – 300 kHz. We acquired 10 data points per frequency decade. Following the EIS measurements of right (lipid-laden) vs. left (control) arteries, the catheter was removed, and the pigs were euthanized with an overdose of pentobarbital and phenytoin. Bilateral carotid arteries were collected for histology and immunostaining for lipid (oxLDL), collagen, smooth muscle cells in the arterial walls.

### 2.4. 3-D EIS-derived EIT mappings from 15 EIS permutations

3-D EIS-derived EIT mappings allowed for endoluminal mapping of conductivity or impedance distributions. Impedance computation was performed at 10 kHz based on the fading of the electrode contact impedance beyond 1 kHz (Supplementary Figure SI-2). This frequency reflected the resistance contribution distinct from the collagen, lipid, and smooth muscle in the arterial wall (Supplementary Table I) while the reactance contribution was negligible.

To reconstruct 3-D EIS-derived EIT mappings, we divided the arterial segments into 864 elements, of which the smooth muscle cell layer was represented by 576 elements (Supplementary Figure SI-5). Assuming each element to be uniform, we derived the initial impedance/conductivity for the smooth muscle from the EIS measurements. We used the conductivity of collagen for the remainder of the elements, and we computed the impedance values for the 15 permutations via the EIDORS (version 3.8) [26]. We incorporated this information and the “genetic algorithm” to alter the conductivity value of each element, and we created a new set of impedance values for the 15 permutations [27,28] (refer to Supplemental SI-5). The conductivity maps were generated by minimizing the impedance difference between the measured and computed data. The details for deriving the conductivity values were provided in Supplementary SI-5.

### 2.5. Histology, immunostaining, and reconstruction of 3-D histology

The carotid arteries with stenosis were dissected into segments at 10 mm in length. The samples were fixed in 10% formalin, dehydrated and embedded in paraffin. Transverse sections were collected from the center with 5 slices on each side at 0.4 mm apart. A total of 11 slices were sectioned, and each slice was further sectioned into thin sections at  $5 \mu\text{m}$  in thickness for (1) Movat staining for the connective tissue,

including elastic fibers (black), collagen and reticular fibers (yellow), fibrin (bright red), and muscle (red) (Supplementary Figure SI-1); (2) Picrosirius Red staining to visualize collagen type I and III fibers (bright red) (Fig. 4B); and (3) E06 immunostaining for oxidized-LDL (oxLDL)-laden lesions (brown) with hematoxylin counterstain (purple) (CV Path Institute, Inc. Gaithersburg, MD, USA) (Fig. 4F).

In addition, we reconstructed the 3-D histology from these 11 slices to model the complete segment of the dissected carotid artery (Supplementary Figure SI-6). The histological slices were aligned using the center of the cross-sectional images, and they were inputted into Image-J software (National Institute of Health, Bethesda, MD, USA). Segmentation of the lumen, media, and adventitia layer was performed in SimVascular, and the gaps between the slices were interpolated using the spline function [29]. The results were exported to Paraview for 3-D visualization [30].

### 2.6. Reconstruction of 3-D histology for finite element modeling to predict EIS measurements

While 3-D mapping identifies the lipid-rich lesions, the number of electrodes influences the spatial resolution of the electrical impedance tomography (EIT). We validated the 3-D EIS profiles via finite element simulation based on the 3-D histology. To simulate the endoluminal topology, we utilized multi-slice histological sections to establish a 3-D model in COMSOL Multiphysics.

As illustrated by the Movat staining (Supplementary SI-1), individual slices from the carotid artery were divided into 3 layers: lumen, inner, and outer arterial wall. The histochemistry analysis revealed that the outer wall was comprised of collagen (Picrosirius Red), the inner wall was mostly smooth muscle cells, and a segment of the inner wall was positive for oxLDL immunostaining in the right but not left carotid arteries (Fig. 4). The 2-D outline of each layer was first extruded from the histological slices in Auto CAD and stacked to reconstruct a 3-D model with the center in alignment with the geometric center of the lumen. We approximated a uniform circle for all cross-sections, and the lumen circumference was estimated from the average circumference of each slice (Supplementary SI-5).

In the absence of any *a priori* knowledge of the precise position of the electrodes relative to each artery, we scanned a wide range of electrode positions to optimally reproduce the measured EIS values. The electrode positions in the cylindrical coordinates corresponded to the distance between the edge of the electrodes and  $z = 0$ ,  $z$ , and to the rotational angle,  $\theta$ . We used 3 different  $z$  values (0, 0.7, and 1.4) and 12 different  $\theta$  values ( $-150^\circ$ ,  $-120^\circ$ ,  $0^\circ$ ,  $30^\circ$ ,  $150^\circ$  and  $180^\circ$ ) to generate 36 possible electrode positions for each arterial model.

The computational EIS model was governed by the Time-Harmonic Maxwell equation. Assuming a negligible contribution from the magnetic field [24], we arrived at the following expression:

$$-\nabla \cdot ((\sigma + j\omega\epsilon_0\epsilon_r)\nabla V) = 0 \quad (1)$$

For each combination of  $z$  and  $\theta$ , 15 impedance values (from the permutations of the 6 electrodes) were solved numerically by using the COMSOL AC/DC module in conjunction with the assigned material properties; namely, conductivity ( $\sigma$ ) and permittivity ( $\epsilon$ ) for the collagen, lipid, and smooth muscle (Supplementary SI-5, Table I).

We reconstructed the individual arterial models from the histology, and we compared between experimental and computational EIS profiles to identify the probable electrode position during the experiments. We adopted the following mathematical criteria for the identification of the closest alignment: the impedance values of the 15 permutations from the experiments were sorted in the following order:  $Z_{exp, 12}$ ,  $Z_{exp, 13}$ ,  $\dots, Z_{exp, 23}$ ,  $\dots, Z_{exp, 34}$ ,  $\dots, Z_{exp, 56}$ . For each permutation in the corresponding simulation results, the impedance values were arranged analogously:  $Z_{sim, 12}$ ,  $Z_{sim, 13}$ ,  $\dots, Z_{sim, 23}$ ,  $\dots, Z_{sim, 34}$ ,  $\dots, Z_{sim, 56}$ . Next, we calculated the summation of the square of the

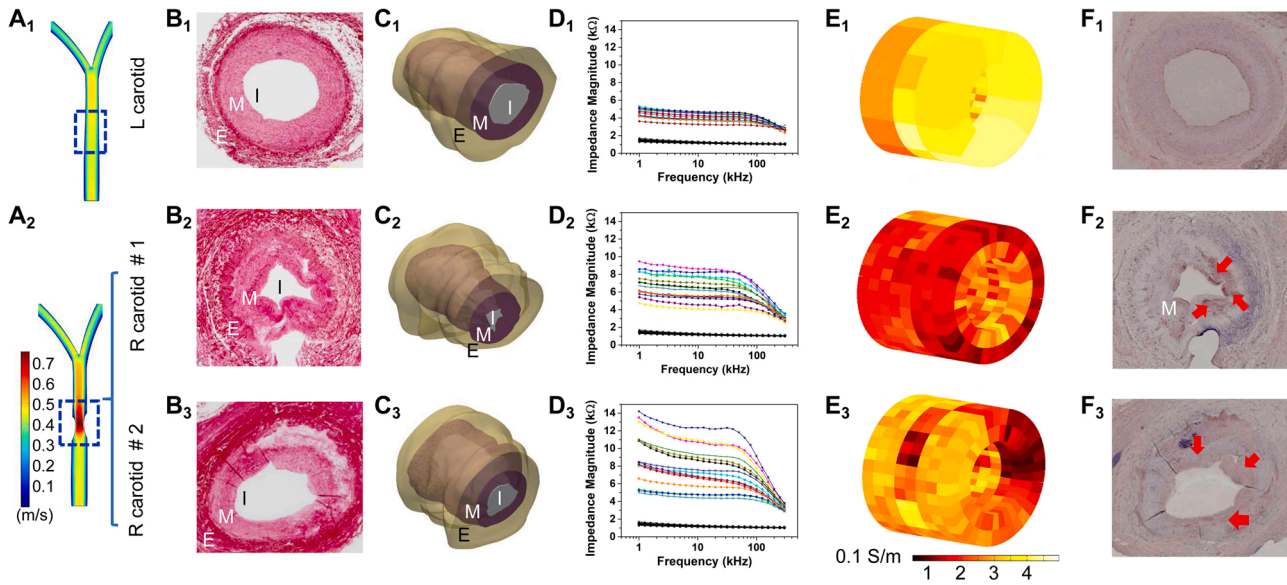


**Fig. 4.** EIS-Derived EIT Roadmap. (A) Velocity streamlines in left carotid arteries (LCA: control) vs. two right carotid arteries (RCA1 and RCA2). (B) Cross-sections of the carotid arteries with Picrosirius Red staining for collagen was compared between the left and right carotid arteries. (C) 3-D reconstruction of right vs. left carotid arteries. The 3-D histological reconstruction recapitulates the endoluminal topology from 11 cross-sections of a segment (4 mm) of carotid arteries. (D) The configuration of the 6-point electrodes (EIS sensor) generates 15 permutations. Frequency-dependent EIS profiles from 1 to 300 kHz were compared between the LCA (control) and two RCAs (RCA1 and RCA2). Baseline EIS profiles (black) were acquired prior to balloon inflation. The individual EIS profiles reflect the 15 permutations. A total of 26 impedance measurements from 1 to 300 kHz were obtained for each EIS profile. (E) 3-D EIS-derived EIT of the tunica intima and tunica media were constructed from the impedance profiles at 10 kHz. (F) The representative E06 staining for oxidized LDL was also compared. The red arrows point to the presence of oxLDL (brown precipitates). I: tunica intima; M: tunica media; E: tunica externa.

differences between the experimental and simulated EIS as follows:

$$\Sigma = \sum_{\substack{ij=1 \\ i \neq j}}^{15} (Z_{exp, ij} - Z_{sim, ij})^2 \quad (2)$$

Then, we defined the deviation as the square root of the summation as follows:

$$\text{Deviation} = \sqrt{\Sigma} \quad (3)$$

The combination of electrode placement resulting in the smallest deviation was taken to be the best fit of the measured impedance values. The selection results were further illustrated through plotting the reciprocal of deviation, as detailed in Figure SI-2.

### 3. Results

#### 3.1. Creating the oxLDL-laden carotid arterial wall in the swine model

Yucatan mini-pigs underwent partial right carotid ligation and were fed a high-fat diet for 16 weeks. All animals were monitored over the 16-week period via CT imaging for the progression of plaque formation in the right carotid arteries (Fig. 3A, D). A 3-D reconstruction from CT scans illustrated the right vs. left carotid artery following right partial ligation (Fig. 2D), revealing the narrowing of the right carotid artery (dotted circle) following 16 weeks of high-fat diet (Fig. 2E). The computational fluid dynamics (CFD) simulation demonstrated the development of disturbed flow downstream from right carotid ligation (Fig. 3B) following the geometric constrains from the partial surgical ligation. As a result, low time-averaged shear stress developed in the regions of disturbed flow to promote plaque formation (Fig. 3C), leading to narrowing of the diameter or known as stenosis in the right carotid arteries (Fig. 3D). Baseline (0 weeks), intermediate (8 weeks), and terminal (16 weeks) diameter measurements of the stenosed right carotid artery (RCA) demonstrated statistically significant narrowing of the right carotid ( $p < 0.05$  vs. left,  $n = 6$ ) (Fig. 3E). The average internal

diameters in the right carotids were reduced by  $\sim 33\%$  (from 4.5 mm to 3 mm), whereas the diameter of the left (control) increased from 4.6 mm to 5.0 mm.

#### 3.2. 3-D EIS-derived EIT of right vs. left carotid arteries

The 3-D EIS sensor was deployed to both the right and left carotid arteries of the Yucatan mini-pigs (Fig. 2). Using the 6-electrode array, we performed 15 intravascular permutations, including 3 permutations to link the vertically aligned electrodes, 6 permutations to link the circumferentially paired, and 6 permutations to link the diagonally paired (Fig. 1D). We measured the baseline EIS profiles in the carotid arteries prior to balloon inflation with electrodes immersed in blood stream (Fig. 4D, black series). Subsequently, 3-D EIS profiles from the corresponding arteries were obtained following balloon inflation. The elevation of EIS profiles indicates specific electrode-tissue contact (Fig. 4D, colored series). We presented two distinct right carotid arteries measurements (RCA1 & RCA2), as compared to left carotid artery (LCA), and the EIS impedance profiles of the RCA were consistently higher than those of LCA (control). Next, we reconstructed the 3-D EIS-derived EIT with the 15 impedance values at 10 kHz for the individual carotid arteries (Fig. 4E). We observed that 3-D EIS mappings were consistent with the histochemistry, as evidenced by E06 staining for oxLDL-laden lumen (Fig. 4F).

The 3 EIT mapping of the LCA (control) shows a yellow to orange color-coded gradient (Figure 4E<sub>1</sub>), indicating the absence of oxLDL (Figure 4F<sub>1</sub>), whereas in RCA1, the dark brown color-coded gradients (Figure 4E<sub>2</sub>) aligned with the prominent semi-circumferential E06 staining (Figure 4F<sub>2</sub>). In RCA2, the dark brown gradients (Figure 4E<sub>3</sub>) correspond to the presence of E06 staining in the right upper quadrant of the carotid circumference (Figure 4F<sub>3</sub>). The prominent oxLDL distribution (Figure 4F<sub>3</sub>) in RCA1 further supported a broader range of impedance profiles (Figure 4D<sub>2</sub>) than that of RCA2 (Figure 4D<sub>3</sub>). Thus, 3-D EIS-derived EIT demonstrated endoluminal mapping of metabolically active arteries.

### 3.3. Computational modeling to validate experimental EIS profiles

3-D histological data were used to develop finite element modeling for validating the EIS profiles. We identified the electrode positions ( $z, \theta$ ) in relation to the lumen by comparing the finite element data with EIS (Fig. 5A). We computed the deviation of finite element data from 3-D EIS profiles for each electrode positions (Supplementary SI-2) and identified the best fit between modeling and 3-D EIS from four experimentally measured profiles: LCA, RCA1, RCA2 (two distinct positions RCA2-A & RCA2-B, Fig. 5B, Supplementary SI-3). The modeling values agreed with the low impedance in LCA (control) as compared to the increased values in both RCA1 and RCA2. We demonstrated that changes in the electrode positions and rotations imparted no significant shifts to the 3-D EIS profiles in LCA from the computational model (Supplementary SI-3A). The model also successfully recapitulated the distributions of impedance measurements in RCA1 and RCA2 arteries with oxLDL-laden plaques, and thus, elevated EIS profiles. Furthermore, the different electrode positions in relation to the oxLDL-laden lumen engendered a distinct distribution of EIS profiles between RCA2-A and RCA2-B (Fig. 5C). In the presence of different electrode positions to the lipid-laden lumens, RCA2 at Position B revealed two distinct regions with broader impedance spectra as compared to RCA2 at Position A, which exhibited an evenly spreading EIS profiles. By scanning through possible electrode positions in our computational model, we identified two combinations of  $z$  and  $\theta$  values for reconstructing the impedance distributions (colored dots in Fig. 5C) that overlapped with the 3-D EIS measurements (colored curves in Fig. 5C) from RCA2 at Position A and RCA2 at Position B, respectively. Computational impedance profiles from additional combinations of electrode position are illustrated in Supplementary SI-2. Overall, our 3-D finite element modeling predicated and validated *in situ* endoluminal EIS mapping of metabolically active plaques.

### 4. Discussion

The unique contribution of our 3-D EIS-derived EIT resides in *in situ*

endoluminal mapping of metabolically active arterial walls [31]. The partial ligation of carotid arteries in the Yucatan mini-pig model on 16 weeks of high-fat diet recapitulated the oxLDL-laden endolumen for 15 intravascular EIS permutations at a given frequency, as corroborated by 3-D histology and immunostaining for lipid, connective tissue, and smooth muscle in the arterial wall. The finite element modeling further simulated impedance distributions to predict and validate the 3-D EIS profiles. Thus, endoluminal EIT mapping provides clinical translation from developing sensors to identifying metabolically active lumen prone to develop acute coronary syndromes or stroke.

Numerous techniques have been developed to detect plaque vulnerability. The standard-of-care technique of angiography, now combined with fractional-flow reserve (FFR) measurements, provides the hemodynamic significance of lesions. However, FFR alone is unable to reveal plaque composition or vulnerability to spontaneous rupture. Non-invasive imaging modalities, including Computed tomography (CT) and magnetic resonance imaging (MRI), identify stenotic lesions, but with inadequate spatial resolution and specificity to metabolically unstable plaques. To acquire high resolution images, Li et al. developed an integrated IVUS and optical coherence tomographic (OCT) catheter [32] to improve plaque characterization; however, OCT is limited by the need for saline solution flushing [32]. The advances in photoacoustics (PA) images the vasa vasorum and intraplaque micro-vessels using high photo-absorption and thermal expansion of blood [33–37]. Nevertheless, PA requires saline flushing and the thermal expansion-generated heat may adversely affect the vulnerable plaque. Near-infrared fluorescence (NIRF) is an emerging approach to detect vascular inflammation [38], and positron emission tomography (PET) imaging uses [ $^{18}\text{F}$ ]-fluorodeoxyglucose ( $^{18}\text{F}$ FDG) to demonstrate metabolic activity [39]. However, NIRF requires the injection of contrast agents and PET imaging needs the injection of radioactive isotopes. Alternatively, microbubble contrast agents are utilized in acoustic angiography to assess lesion microvasculature [40–43]; nevertheless, the need for cessation of blood flow during this procedure entails safety issue for clinical application. In this context, 3-D EIS mapping provides the label-free detection for the metabolically active lesions.

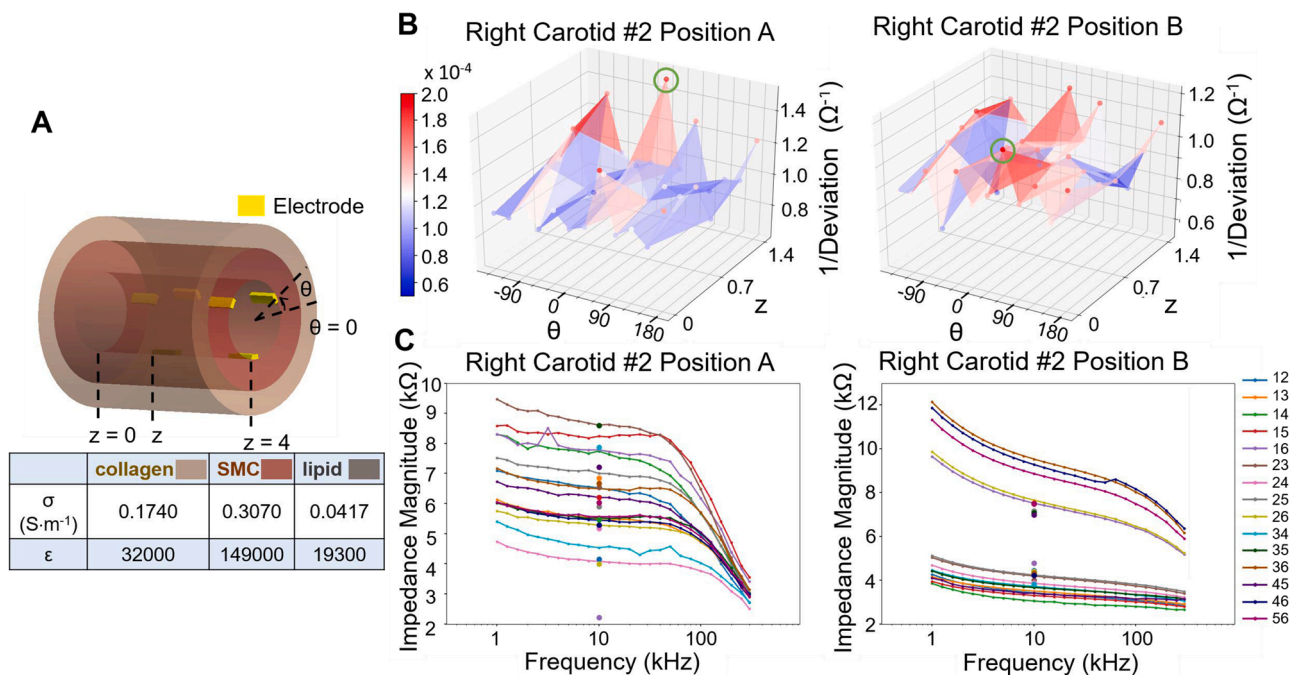


Fig. 5. Comparing the Computational with Measured EIS Profiles. (A) The position of the electrodes in the 3-D model is defined by the polar coordinates, where  $z$  is defined as the distance between the edge of the electrodes and  $z = 0$ , and  $\theta$  is the angle subscribed between the midpoint of the first pair of the electrodes and the  $\theta = 0$ . (B) The 3-D deviation plots showed the best fit of the electrode placement in the simulation model. The electrode position that resulted in the largest reciprocal of the deviation was circled in green. (C) The 15 impedance profiles were compared between two different rotational positions of the electrodes from the same lumen.

3-D Intravascular EIS has the capability of identifying oxLDL-laden foam cells in the subendothelial layers of atherosclerotic lesions. To this end, we demonstrated the capability of 3-D EIS-derived EIT for detecting the gradients of lipid-laden endolumen in the mini-pig model. While we have previously deployed the EIS sensor to detect the fatty streaks in the *ex vivo* human arch and the atherosclerotic lesions in the New Zealand White rabbit model [1–3,21], we created the oxLDL carotid arteries in the mini-pigs with the comparable diameters (3–5 mm) to human coronary arteries [44]. The partial ligation of right carotid arteries, followed by diet-induced hyperlipidemia, accelerated the development of metabolically active plaques that are reported to embolize to the cerebral vascular plexuses as a mode for predicting stroke [31]. Thus, we were able to demonstrate the clinical feasibility of EIT to detect vulnerable plaque prone that may be prone to rupture in the swine model.

To demonstrate 3-D EIT, we directly solved the forward problem by obviating the inverse ill-posed problem encountered by other EIT algorithms [24,45–47]. We used the “genetic algorithm” to optimize the conductivity distributions that were closely overlapping with the Picrosirius Red staining for connective tissue and E06 staining for oxLDL, as represented by the color-coded gradients of 3-D mapping (Fig. 4) [27, 28]. For these reasons, EIT enables the detection of the oxidized LDL in the arterial walls during a diagnostic angiogram.

Our histological segmentation and 3-D reconstruction of the carotid arteries further allowed for the finite element modeling and for validation of the measured EIS profiles. Electrical impedance values are governed by the distinct tissue composition and precise boundary conditions of the organ system [2], and insufficient knowledge of arterial wall composition and topography may deviate the computational modeling from the experimental measurement [48]. In this context, we obtained multi-slice and axial histology to establish a 3-D arterial computational model with well-defined layers of tissue properties ( $\sigma$  = tissue conductivity and  $\epsilon$  = permittivity), including collagen, fatty tissue, and smooth muscle (Supplementary Table I). In the computational model, we simulated the changes in the electrode positions in relation to the arterial wall. Based on observations from the multi-slice histology, the semi-circular region of the arterial wall with the prominent oxLDL staining (Fig. 4) likely contributed to the increase in impedance. By comparing the positions of the electrodes in the cylindrical coordinates ( $z$ ,  $\theta$ ), we identified two distinct electrode positions to reconstruct a comparable impedance distribution from two oxLDL-laden carotid arteries (Fig. 5). Hence, the computational models simulated two different electrode positions to predict and validate the 3-D EIS measurements.

Both EIT mapping and finite element modeling are complementary to detecting the endoluminal metabolic state. However, effective reconstruction of the 3-D EIS-derived EIT depends on the number of electrodes. The current 6-electrode configuration may be expanded to 12 electrodes for enhanced spatial resolution. While increasing the number of electrodes would require additional computation for tomographic reconstruction, our current methodology provides a foundation for this future step. Furthermore, our computational model has provided validation of our experimental EIS measurements. With the *a priori* knowledge of the boundary condition and histology, the computational model simulated the changes in electrode positions from two separate EIS measurements; thus, validating the current 6-point electrode configuration to map the oxLDL-rich endolumen.

Taken together, we demonstrate the translational capability of 3-D multi-electrode configuration to detect the metabolically active endolumen in the pre-clinical model of unstable plaques. Our 3-D EIS-derived EIT is consistent with the 3-D histology in the Yucatan mini-pigs, demonstrating the detection of oxidized LDL-laden plaques. Future studies will aim to calibrate the 3-D EIS gradients with the extent of lipid core for advancing our clinical understanding of the vulnerable plaque with translational implications in interventions aimed at plaque modification.

## Funding

This project was supported by NIH R01HL111437 (T.K.H.), R01HL118650 (T.K.H.), R01HL149808 (T.K.H.), NIGMS GM008042 (PA) and UCLA David Geffen Scholarship (P.A.).

## CRedit authorship contribution statement

**Parinaz Abiri:** Conceptualization, Methodology, Writing – original draft. **Yuan Luo:** Conceptualization, Methodology, Writing – original draft. **Zi-Yu Huang:** Conceptualization, Methodology, Writing – original draft. **Qingyu Cui:** Visualization, Writing – review & editing, Validation. **Sandra Duarte-Vogel:** Investigation. **Mehrdad Roustaei:** Visualization, Investigation. **Chih-Chiang Chang:** Writing – review & editing. **Xiao Xiao:** Visualization, Writing – review & editing. **Rene Packard:** Writing – review & editing. **Susana Cavallero:** Resources, Writing – review & editing. **Ramin Ebrahimi:** Writing – review & editing. **Peyman Benharash:** Writing – review & editing. **Jun Chen:** Writing – review & editing. **Yu-Chong Tai:** Supervision, Writing – review & editing. **Tzung K. Hsiai:** Funding acquisition, Project administration, Supervision, Writing – review & editing.

## Declaration of Competing Interest

The authors declare that they have no known competing financial interests or personal relationships that could have appeared to influence the work reported in this paper.

## Acknowledgments

We appreciate Chadi Nahal for sorting the histological data

## Appendix A. Supporting information

Supplementary data associated with this article can be found in the online version at [doi:10.1016/j.snb.2021.131152](https://doi.org/10.1016/j.snb.2021.131152).

## References

- [1] H. Cao, F. Yu, Y. Zhao, N. Scianmarello, J. Lee, W. Dai, N. Jen, T. Beebe, R. Li, R. Ebrahimi, D.S. Chang, F.V. Mody, J. Pacella, Y.-C. Tai, T.K. Hsiai, Stretchable electrochemical impedance sensors for intravascular detection of lipid-rich lesions in New Zealand White rabbits, *Biosens. Bioelectron.* 54 (2014) 610–616.
- [2] F. Yu, X. Dai, T. Beebe, T.K. Hsiai, Electrochemical impedance spectroscopy to characterize inflammatory atherosclerotic plaques, *Biosens. Bioelectron.* 30 (1) (2011) 165–173.
- [3] F. Yu, J. Lee, N. Jen, X. Li, Q. Zhang, R. Tang, Q. Zhou, E.S. Kim, T.K. Hsiai, Elevated electrochemical impedance in the endoluminal regions with high shear stress: Implication for assessing lipid-rich atherosclerotic lesions, *Biosens. Bioelectron.* 43 (2013) 237–244.
- [4] B. Mihaylova, J. Emberson, L. Blackwell, A. Keech, J. Simes, E.H. Barnes, M. Voysey, A. Gray, R. Collins, C. Baigent, The effects of lowering LDL cholesterol with statin therapy in people at low risk of vascular disease: meta-analysis of individual data from 27 randomised trials, *Lancet* 380 (9841) (2012) 581–590. Epub 2012/05/23. PubMed PMID: 22607822; PMCID: PMC3437972.
- [5] P.G. Steg, M. Szarek, D.L. Bhatt, V.A. Bittner, M.F. Brégeault, A.J. Dalby, R. Diaz, J. M. Edelberg, S.G. Goodman, C. Hanotin, R.A. Harrington, J.W. Jukema, G. Lecorps, K.W. Mahaffey, A. Moryusef, P. Ostadal, A. Parkhomenko, R. Pordy, M.T. Roe, P. Tricoci, R. Vogel, H.D. White, A.M. Zeiher, G.G. Schwartz, Effect of alirocumab on mortality after acute coronary syndromes, *Circulation* 140 (2) (2019) 103–112. Epub 2019/05/24. PubMed PMID: 31117810; PMCID: PMC6661243.
- [6] E.A. Bohula, S.D. Wiviott, R.P. Giugliano, M.A. Blazing, J.G. Park, S.A. Murphy, J. A. White, F. Mach, F. Van de Werf, A.J. Dalby, H.D. White, A.M. Tershakovec, C. P. Cannon, E. Braunwald, Prevention of stroke with the addition of ezetimibe to statin therapy in patients with acute coronary syndrome in IMPROVE-IT (improved reduction of outcomes: vytorin efficacy international trial), *Circulation* 136 (25) (2017) 2440–2450. Epub 2017/10/04. PubMed PMID: 28972004.
- [7] L.H. Arroyo, R.T. Lee, Mechanisms of plaque rupture, *Cardiovasc. Res.* 41 (2) (1999) 369–375.
- [8] B.J. Maron, W.J. McKenna, G.K. Danielson, L.J. Kappenberger, H.J. Kuhn, C. E. Seidman, P.M. Shah, W.H. Spencer III, P. Spirito, Ten, F.J. Cate, American College of Cardiology/European Society of Cardiology clinical expert consensus document on hypertrophic cardiomyopathy: a report of the American College of Cardiology Foundation Task Force on Clinical Expert Consensus Documents and

- the European Society of Cardiology Committee for Practice Guidelines, *J. Am. Coll. Cardiol.* 42 (9) (2003) 1687–1713.
- [9] A.P. Burke, A. Farb, G.T. Malcom, Y.-h Liang, J. Smialek, R. Virmani, Coronary risk factors and plaque morphology in men with coronary disease who died suddenly, *N. Engl. J. Med.* 336 (18) (1997) 1276–1282.
- [10] H.M. García-García, B.D. Gogas, P.W. Serruys, N. Bruining, IVUS-based imaging modalities for tissue characterization: similarities and differences, *Int. J. Cardiovasc. Imaging* 27 (2) (2011) 215–224.
- [11] F.D. Kolodgie, A.P. Burke, A. Farb, H.K. Gold, J. Yuan, J. Narula, A.V. Finn, R. Virmani, The thin-cap fibroatheroma: a type of vulnerable plaque: the major precursor lesion to acute coronary syndromes, *Curr. Opin. Cardiol.* 16 (5) (2001) 285–292.
- [12] T. Kume, H. Okura, R. Yamada, T. Kawamoto, N. Watanabe, Y. Neishi, Y. Sadahira, T. Akasaka, K. Yoshida, Frequency and spatial distribution of thin-cap fibroatheroma assessed by 3-vessel intravascular ultrasound and optical coherence tomography, *Circ. J.* 73 (2009) 1086–1091, 0903310317-.
- [13] F. Prati, E. Regar, G.S. Mintz, E. Arbustini, C. Di Mario, I.-K. Jang, T. Akasaka, M. Costa, G. Guagliumi, E. Grube, Expert review document on methodology, terminology, and clinical applications of optical coherence tomography: physical principles, methodology of image acquisition, and clinical application for assessment of coronary arteries and atherosclerosis, *Eur. Heart J.* 31 (4) (2010) 401–415.
- [14] G.A. Rodríguez-Granillo, H.M. García-García, E.P. Mc Fadden, M. Valgimigli, J. Aoki, P. de Feyter, P.W. Serruys, In vivo intravascular ultrasound-derived thin-cap fibroatheroma detection using ultrasound radiofrequency data analysis, *J. Am. Coll. Cardiol.* 46 (11) (2005) 2038–2042.
- [15] H. Yabushita, B.E. Bouma, S.L. Houser, H.T. Aretz, I.-K. Jang, K.H. Schlendorf, C. R. Kauffman, M. Shishkov, D.-H. Kang, E.F. Halpern, Characterization of human atherosclerosis by optical coherence tomography, *Circulation* 106 (13) (2002) 1640–1645.
- [16] O. Ghekieire, R. Salgado, N. Buls, T. Leiner, I. Mancini, P. Vanhoenacker, P. Dendale, A. Nchimi, Image quality in coronary CT angiography: challenges and technical solutions, *Br. J. Radiol.* 90 (1072) (2017) 20160567. Epub 2017/01/06. PubMed PMID: 28055253; PMCID: PMC5605061.
- [17] J. Tanabe, M. Tanaka, K. Kadooka, H. Hadeishi, Efficacy of high-resolution cone-beam CT in the evaluation of carotid atheromatous plaque, *J. Neurointerv. Surg.* 8 (3) (2016) 305–308. Epub 2015/01/24. PubMed PMID: 25613682.
- [18] M. Chiochi, A. Chiaravalloti, D. Morosetti, G. Loreni, R. Gandini, S. Mancino, S. Fabiano, G. Simonetti, Virtual histology-intravascular ultrasound as a diagnostic alternative for morphological characterization of carotid plaque: comparison with histology and high-resolution magnetic resonance findings, *J. Cardiovasc. Med. (Hagerstown, Md)* 20 (5) (2019) 335–342. Epub 2019/03/30. PubMed PMID: 30925146.
- [19] Li J, Montarello NJ, Hoogendoorn A, Verjans JW, Bursill CA, Peter K, Nicholls SJ, McLaughlin RA, Psaltis PJ. Multimodality Intravascular Imaging of High-Risk Coronary Plaque. *JACC Cardiovascular imaging.* 2021. Epub 2021/05/24. PubMed PMID: 34023267.
- [20] L. Marcu, J.A. Jo, Q. Fang, T. Papaioannou, T. Reil, J.H. Qiao, J.D. Baker, J. A. Freischlag, M.C. Fishbein, Detection of rupture-prone atherosclerotic plaques by time-resolved laser-induced fluorescence spectroscopy, *Atherosclerosis* 204 (1) (2009) 156–164. Epub 2008/10/18. PubMed PMID: 18926540; PMCID: PMC2766393.
- [21] F. Yu, R. Li, L. Ai, C. Edington, H. Yu, M. Barr, E. Kim, T.K. Hsiai, Electrochemical impedance spectroscopy to assess vascular oxidative stress, *Ann. Biomed. Eng.* 39 (1) (2011) 287–296.
- [22] I. Streitner, M. Goldhofer, S. Cho, R. Kinscherf, H. Thielecke, M. Borggreffe, T. Süselbeck, F. Streitner, Cellular imaging of human atherosclerotic lesions by intravascular electric impedance spectroscopy, *PLoS One* 7 (4) (2012), e35405. Epub 2012/04/18. PubMed PMID: 22509411; PMCID: PMC3324547.
- [23] I. Streitner, M. Goldhofer, S. Cho, H. Thielecke, R. Kinscherf, F. Streitner, J. Metz, K.K. Haase, M. Borggreffe, T. Süselbeck, Electric impedance spectroscopy of human atherosclerotic lesions, *Atherosclerosis* 206 (2) (2009) 464–468. Epub 2009/05/08. PubMed PMID: 19419719.
- [24] D.S. Holder, *Electrical Impedance Tomography: Methods, History and Applications*, CRC Press, 2004.
- [25] J. Hwang, M.H. Ing, A. Salazar, B. Lassègue, K. Griendling, M. Navab, A. Sevanian, T.K. Hsiai, Pulsatile versus oscillatory shear stress regulates NADPH oxidase subunit expression: implication for native LDL oxidation, *Circ. Res.* 93 (12) (2003) 1225–1232.
- [26] A. Adler, A. Boyle, M.G. Crabb, H. Gagnon, B. Grychtol, N. Lesparre, W.R. Lionheart, editors. EIDORS Version 3.8. Proc of the 16th Int Conf on Biomedical Applications of Electrical Impedance Tomography; 2015.
- [27] M. Kumar, M. Husain, N. Upreti, D. Gupta. Genetic algorithm: Review and application. Available at SSRN 3529843. 2010.
- [28] V.P. Rolnik, P. Selegim Jr., A specialized genetic algorithm for the electrical impedance tomography of two-phase flows, *J. Braz. Soc. Mech. Sci. Eng.* 28 (4) (2006) 378–389.
- [29] A. Updegrave, N.M. Wilson, J. Merkow, H. Lan, A.L. Marsden, S.C. Shadden, SimVascular: an open source pipeline for cardiovascular simulation, *Ann. Biomed. Eng.* 45 (3) (2017) 525–541.
- [30] J. Ahrens, B. Geveci, C. Law, editors. ParaView: An End-User Tool for Large-Data Visualization. The Visualization Handbook; 2005.
- [31] Z.-S. Shi, L. Peng, X. He, A. Ishii, J. Goldstine, H. Vinters, F. Vinuela, Vulnerable plaque in a Swine model of carotid atherosclerosis, *Am. J. Neuroradiol.* 30 (3) (2009) 469–472.
- [32] B. Lei, G.R. Li, X.P. Gao, Morphology dependence of molybdenum disulfide transparent counter electrode in dye-sensitized solar cells, *J. Mater. Chem. A* 2 (11) (2014) 3919–3925.
- [33] B. Wang, J.L. Su, A.B. Karpouk, K.V. Sokolov, R.W. Smalling, S.Y. Emelianov, Intravascular photoacoustic imaging, *IEEE J. Sel. Top. Quantum Electron.* 16 (3) (2010) 588–599.
- [34] L.V. Wang, Multiscale photoacoustic microscopy and computed tomography, *Nat. Photon.* 3 (9) (2009) 503–509.
- [35] L.V. Wang, S. Hu, Photoacoustic tomography: in vivo imaging from organelles to organs, *Science* 335 (6075) (2012) 1458–1462.
- [36] R. Weissleder, C.-H. Tung, U. Mahmood, A. Bogdanov, In vivo imaging of tumors with protease-activated near-infrared fluorescent probes, *Nat. Biotechnol.* 17 (4) (1999) 375–378.
- [37] M. Xu, L.V. Wang, Photoacoustic imaging in biomedicine, *Rev. Sci. Instrum.* 77 (4) (2006), 041101.
- [38] R. Weissleder, C.-H. Tung, U. Mahmood, A. Bogdanov, In vivo imaging of tumors with protease-activated near-infrared fluorescent probes, *Nat. Biotechnol.* 17 (4) (1999) 375–378.
- [39] J.H. Rudd, E. Warburton, T. Fryer, H. Jones, J. Clark, N. Antoun, P. Johnström, A. Davenport, P. Kirkpatrick, B.N. Arch, Imaging atherosclerotic plaque inflammation with [18F]-fluorodeoxyglucose positron emission tomography, *Circulation* 105 (23) (2002) 2708–2711.
- [40] R. Gessner, M. Lukacs, M. Lee, E. Cherin, F.S. Foster, P.A. Dayton, High-resolution, high-contrast ultrasound imaging using a prototype dual-frequency transducer: in vitro and in vivo studies, *IEEE Trans. Ultrason. Ferroelectr. Freq. Control* 57 (8) (2010) 1772–1781.
- [41] R.C. Gessner, C.B. Frederick, F.S. Foster, P.A. Dayton, Acoustic angiography: a new imaging modality for assessing microvasculature architecture, *Int. J. Biomed. Imaging* 2013 (2013), 936593.
- [42] J.R. Lindner, Microbubbles in medical imaging: current applications and future directions, *Nat. Rev. Drug Discovery* 3 (6) (2004) 527–533.
- [43] J.R. Lindner, J. Song, A.R. Jayaweera, J. Sklenar, S. Kaul, Microvascular rheology of Definity microbubbles after intra-arterial and intravenous administration, *J. Am. Soc. Echocardiogr.* 15 (5) (2002) 396–403.
- [44] F.-F. Zhou, Liu Y-h, Ge. P.-C. Chen, Z.-H. Ding, X.-Q. Liu, J.-Y. Jia, Q.-W. An, F.-H. Li, L.-H. Wang, L.-S. Coronary artery diameter is inversely associated with the severity of coronary lesions in patients undergoing coronary angiography, *Cellular Physiology and Biochemistry* 43 (3) (2017) 1247–1257.
- [45] A. Adler, A. Boyle, Electrical impedance tomography: tissue properties to image measures, *IEEE Trans. Biomed. Eng.* 64 (11) (2017) 2494–2504.
- [46] Y. Luo, P. Abiri, S. Zhang, C.-C. Chang, A.H. Kaboodrangi, R. Li, A.K. Sahib, A. Bui, R. Kumar, M. Woo, Non-invasive electrical impedance tomography for multi-scale detection of liver fat content, *Theranostics* 8 (6) (2018) 1636–1647.
- [47] C.C. Chang, Z.-Y. Huang, S.F. Shih, Y. Luo, A. Ko, Q. Cui, J. Sumner, S. Cavallero, S. Das, W. Gao, J. Sinsheimer, A. Bui, J.P. Jacobs, P. Pajukanta, H. Wu, Y.C. Tai, Z. Li, T.K. Hsiai, Electrical impedance tomography for non-invasive identification of fatty liver infiltrate in overweight individuals, *Sci. Rep.* 11 (1) (2021) 19859. Epub 2021/10/08. PubMed PMID: 34615918; PMCID: PMC8494919.
- [48] R.R.S. Packard, Y. Luo, P. Abiri, N. Jen, O. Aksoy, W.M. Suh, Y.-C. Tai, T.K. Hsiai, 3-D electrochemical impedance spectroscopy mapping of arteries to detect metabolically active but angiographically invisible atherosclerotic lesions, *Theranostics* 7 (9) (2017) 2431–2442.

**Parinaz Abiri** received her MD/PhD from UCLA Schools of Engineering and Medicine, Los Angeles, CA, USA

**Yuan Luo**, PhD, is currently an Assistant Professor of Biomedical Engineering at Southern University of Science and Technology, Shenzhen, Guangdong, China

**Zi-Yu Huang** is a PhD student in Department of Medical Engineering, California Institute of Technology, Pasadena, CA.

**Quinyu Cui**, PhD, is a post-doctoral fellow in the Division of Cardiology, Department of Medicine, David Geffen School of Medicine, University of California, Los Angeles, Los Angeles, CA

**Sandra Duarte-Vogel**, DMV, is our veterinarian attending in the Department of Laboratory Animal Research at UCLA

**Mehrdad Roustaei** is a PhD student in the Department of Bioengineering, UCLA, CA

**Chih-Chiang Chang** is a PhD student in the Department of Bioengineering, UCLA, CA

**Xiao Siao** is a PhD student in the Department of Bioengineering, UCLA, CA

**Rene S. Packard**, MD, PhD, is the Assistant Professor of Medicine in the Division of Cardiology, Department of Medicine, David Geffen School of Medicine, University of California, Los Angeles, Los Angeles, CA

**Susana Cavallero**, PhD, is a project scientist in the Division of Cardiology, Department of Medicine, David Geffen School of Medicine, University of California, Los Angeles, Los Angeles, CA

**Ramin Ebrahimi**, MD, is the Interventional Cardiologist in the Greater Los Angeles VA Healthcare System, Los Angeles, CA

**Jun Chen**, PhD, is the Assistant Professor of Bioengineering in the Department of Bioengineering, University of California, Los Angeles, Los Angeles, CA.

**Yu-Chong Tai**, PhD, is the Chair and Professor of Electrical and Medical Engineering in the Department of Medical Engineering, California Institute of Technology, Pasadena, CA.

**Tzung K. Hsiai**, MD, PhD, is the Professor of Medicine and Bioengineering in the scientist in the Division of Cardiology, Department of Medicine, David Geffen School of Medicine, University of California, Los Angeles, Los Angeles, CA